

X-ray scattering from liquid interfaces

LI Ming¹ Mark L. SCHLOSSMAN²*(¹Beijing National Laboratory for Condensed Matter Physics, Institute of Physics,**Chinese Academy of Sciences, Beijing 100080, China;**²Departments of Physics and Chemistry, University of Illinois at Chicago, 845 W. Taylor St, Chicago, IL 60607, USA)*

Abstract Synchrotron radiation X-ray scattering is a useful tool for structural characterization of liquid interfaces. Specular reflectivity provides precise measurement of the interfacial widths and of the ordering of surfactants adsorbed to these interfaces. Diffuse scattering gives information on phase transitions and domain formation in surfactant monolayers and on interfacial fluctuations confined by and coupled across fluidic films.

Key words Liquid interfaces; X-ray scattering; Synchrotron radiation

CLC numbers O434.1, O436.2, O647.11

1 Introduction

The structure of liquid interfaces is relevant to the understanding of electron and molecular transfer across biological membranes and to the partitioning of solvents and metal ions. Also, liquid interfaces are model systems whose study influences the understanding of inhomogeneous materials. In spite of their importance, there remain fundamental questions in the study of liquid interfaces. For example, there is currently a poor understanding of molecular ordering near and within the interface. This understanding has been impeded by the lack of structural probes of the interface on the molecular length scale. Small angle neutron or X-ray scattering, dynamic light scattering, and other techniques have been traditionally used to study the internal domains in surfactant solutions. A more recent object of study is a single, macroscopic, nearly planar liquid interface. This provides an oriented system for study using experimental techniques sensitive primarily to the interfacial structure.

Of equal importance is the structure of phospholipid bilayers in the fluid state, which is relevant to many life processes. Bilayers can, in principle, be treated as a stack of fluidic membranes with many

internal interfaces. Conventionally, structural analysis of these bilayers has employed the approach of crystallographic X-ray diffraction of multilamellar membranes. However, if fully hydrated, fluidic lipid membrane arrays do not have enough diffraction peaks for crystallographic analysis. In this case, the hard solid-liquid interface provides an indispensable environment for the study of multilamellar membranes. When deposited on solid substrates, their structure can be easily studied by modern interface-sensitive scattering techniques that utilize synchrotron X-rays. A high degree of orientation makes possible a precise distinction between the scattering vector component normal and parallel to the bilayer, allowing for the study of the lateral structure of the bilayers. Furthermore, the solid surface effectively reduces the thermal fluctuations, making it possible to determine electron density profiles with high resolution, even in fully hydrated states.

In this article, certain recent studies are reviewed on liquid interfaces using synchrotron radiation X-rays. A brief introduction is provided regarding the theory and experimental methods of X-scattering from liquid interfaces. The kinetic theory is adopted because it is

easy to understand. Certain mathematical derivations of correlation functions, essential to understand the physics involved in this review, are also discussed.

2 Theoretical background

The scattering from interfaces of electromagnetic waves in the X-ray region is basically the same as the scattering of visible light electromagnetic waves from material surfaces. The difference lies in the length scales probed by the radiation. X-ray scattering is a probe to investigate surfaces on the nanometer scale, while visible light determines structural information on lengths of the order of micrometers. X-rays can be specularly reflected by a smooth surface, just as light is reflected by a mirror. If the surface is rough, photons are diffusely scattered in off-specular directions. Total external reflection can occur for both X-rays and visible light. This is understandable because for X-rays, the refraction index of a medium is slightly less than one. The higher the electron density (defined as the total number of electrons per unit volume), the lower the refraction index. From basic optics, it is known that an electromagnetic wave will be totally reflected when it enters a low index medium from a high index medium at a grazing angle α_i less than the critical angle α_c . In the X-ray literature, all angles are measured toward the surface and not, as in visible light optics, with respect to the surface normal (Fig. 1).

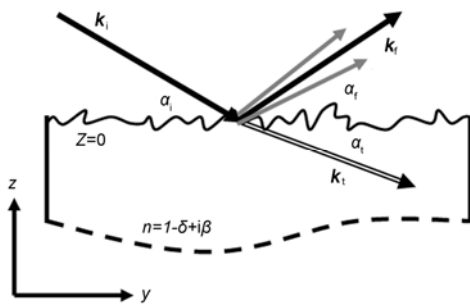


Fig.1 A plane electromagnetic wave with wave-vector \mathbf{k}_i is incident upon a surface at grazing angle α_i . The wave splits into two main waves, i.e., a reflected one at $\alpha_r (= \alpha_i)$ and a refracted one at α_t . The diffusely scattered photons near the reflected waves are also indicated (gray lines).

The theory of X-ray scattering from interfaces can be presented within the kinetic approximation, similar to kinetic treatments of X-ray diffraction. In order for this article to be easily understood by even a

beginner, the kinetic approximation (also known as the Born approximation in the theory of particle scattering) has been used to derive the formula used in this article and the interested readers are referred to two books [1,2]. The kinetic theory of X-ray scattering breaks down in the region near the critical angle. Therefore, it cannot explain those phenomena related to total external reflection. Fortunately, use of the kinetic approximation will not affect the understanding of the problems presented in the current review. A brief interpretation is given and readers can refer to the relevant literature.

X-ray scattering occurs from a solid surface (Fig. 1). The differential cross section of X-ray scattering of a medium is proportional to the Fourier transform of the electron density profile $\rho(r)$ of the medium,

$$\frac{d\sigma}{d\Omega} = \left| r_e \int_V d^3R \rho(\mathbf{R}) e^{iq \cdot \mathbf{R}} \right|^2 \quad (1)$$

where $r_e = e^2 / mc^2$ is the Thomson scattering length of the electron, $q \equiv \mathbf{k}_f - \mathbf{k}_i$ is the scattering vector (also called the momentum transfer), and integration is over the volume of the medium. $\rho(r)$ is defined as the number of electrons per unit volume. In the case of X-ray scattering from surfaces and interfaces, one is usually interested in small angle scattering for which the details of the electron distribution around the lattice are beyond the resolving power of the X-rays. To a good approximation, bulk phases appear to X-rays as uniformly charged, with interfaces being the only relevant inhomogeneities.

For large positive or negative values of z (Fig. 1), the electron density is constant and equal to the bulk value for the corresponding phase. This suggests rewriting Eq. (1) in terms of the derivative of electron density with respect to z :

$$\begin{aligned} \frac{d\sigma}{d\Omega} &= \left| \frac{r_e}{iq_z} \int_{-\infty}^{+\infty} d^2r dz \frac{\partial \rho(r,z)}{\partial z} e^{iq_z h(r)} e^{iq_{xy} \cdot r} \right|^2 \\ &= \frac{r_e^2 \Delta \rho^2 |\Phi(q_z)|^2}{q_z^2} \int_{-\infty}^{+\infty} d^2r d^2r' e^{iq_z (h(r)-h(r'))} e^{iq_{xy} \cdot (r-r')} \end{aligned} \quad (2)$$

where $h(r)$ is the local position of the interface above the mean plane $\bar{z} = 0$, $\Delta \rho$ is the difference between the electron densities of the two bulk phases, and $\Phi(q_z)$ is the one-dimensional Fourier transform of $\partial \rho / \partial z$. The footprint of the X-ray beam is assumed to be smaller than the interface (so that the integration is extended to infinity).

The intensity measured in an experiment is the statistical average of Eq. (2) due to the finite X-ray coherence length. Therefore,

$$\frac{d\sigma}{d\Omega} = A_s r_e^2 \Delta\rho^2 \frac{|\Phi(q_z)|^2}{q_z^2} \int_{-\infty}^{+\infty} d^2r \langle e^{iq_z(h(r)-h(0))} \rangle e^{iq_{xy}\cdot r} \quad (3)$$

where A_s is the area of the interface exposed to the X-ray beam. Eq. (3) is not valid if coherent X-rays are scattered by solid surfaces. A speckle pattern will be observed in such a case [3]. But this is not a concern for liquid interfaces which are constantly fluctuating. The X-ray scattering data are normally collected over time intervals much larger than the temporal correlation between subsequent interfacial configurations. Eq. (3) can be understood as a time average. The interface is assumed to be homogeneous and isotropic so that the average $\langle \exp[iq_z(h(r)-h(0))] \rangle$ depends only on the distance between the two points. Suppose $[h(r)-h(0)]$ is a Gaussian random variable, then

$$\langle e^{iq_z(h(r)-h(0))} \rangle = e^{-0.5q_z^2 g(r)} \quad (4)$$

where $g(r) = \langle (h(r)-h(0))^2 \rangle$ is the height-difference correlation function, which can be expressed in terms of the interfacial roughness σ (defined by $\sigma^2 = \langle h(0)^2 \rangle$) and the height-height correlation function of interfacial fluctuations, $C(r) = \langle h(0)h(r) \rangle$. The correlation function is given by

$$g(r) = 2(\sigma^2 - C(r)) \quad (5)$$

and Eq. (3) becomes

$$\frac{d\sigma}{d\Omega} = A_s r_e^2 \Delta\rho^2 |\Phi(q_z)|^2 \frac{e^{-q_z^2 \sigma^2}}{q_z^2} \int_{-\infty}^{+\infty} d^2r e^{q_z^2 C(r)} e^{iq_{xy}\cdot r} \quad (6)$$

Eq. (6) can be split into two parts:

$$\left(\frac{d\sigma}{d\Omega} \right)_{\text{spec}} = A_s r_e^2 \Delta\rho^2 |\Phi(q_z)|^2 \frac{e^{-q_z^2 \sigma^2}}{q_z^2} (2\pi)^2 \delta(\mathbf{q}_{xy}) \quad (7)$$

$$\left(\frac{d\sigma}{d\Omega} \right)_{\text{diff}} = A_s r_e^2 \Delta\rho^2 |\Phi(q_z)|^2 \frac{e^{-q_z^2 \sigma^2}}{q_z^2} \int_{-\infty}^{+\infty} d^2r (e^{q_z^2 C(r)} - 1) e^{iq_{xy}\cdot r} \quad (8)$$

where the specular reflection in Eq. (7) is identified by the delta function and Eq. (8) describes the nonspecular diffuse scattering.

To compare the theory with measured data, Eq. (6) should be integrated over the solid angle corresponding to the detector's angular acceptance $\Delta\Omega$, that is,

$$I(\mathbf{q}) = (I_o / A_s \sin \alpha) \int_{\Delta\Omega} d\Omega (d\sigma / d\Omega) \quad (9)$$

The factor $\sin \alpha$ converts between the beam's cross-sectional area and its footprint on the sample surface. In specular reflection, $\alpha = \beta$. The solid angle element $d\Omega$ can be written as $d\Omega = dq_x dq_y / (k^2 \sin \beta)$, and the intensity $I_{\text{spec}}(0,0,q_z)$ has a pre-factor $1/q_z^4$, which is in agreement with that given by the standard electromagnetic treatment for large q_z .

The above-mentioned equations can be readily extended to the scattering from multiple interfaces:

$$\frac{d\sigma}{d\Omega} \propto r_e^2 \sum_{j,k=1}^N \frac{\Delta\rho_j \Delta\rho_k}{q_z^2} e^{-0.5q_z^2(\sigma_j^2 + \sigma_k^2)} e^{iq_z(z_j - z_k)} \int_{-\infty}^{+\infty} d^2r e^{q_z^2 C_{jk}(r)} e^{iq_{xy}\cdot r} \quad (10)$$

where $C_{jk}(r)$ is the intercorrelation function between interfaces j and k (Fig. 2). Here, a new concept is introduced. It is the so-called resonant diffuse scattering which occurs when the fluctuations of the interfaces are correlated (or conformal). Figs. 2(a) and 2(b) are, respectively, examples of correlated and uncorrelated interfaces. The resonant diffuse scattering results when the diffusely scattered waves from different interfaces are in phase so that the diffuse scattering is concentrated at the Bragg sheets in the reciprocal space (Fig. 2). A Bragg sheet is a plane with constant q_z at which the Bragg condition is satisfied. This is seen mathematically from Eq. (10): one observes resonant diffuse scattering when $C_{jk}(r) \neq \delta_{j,k}$.

3 Experimental techniques

The scattering geometry has already been illustrated in Fig. 1. The experiment measures the distribution of the scattering intensity in reciprocal space, namely, \mathbf{q} -space. The scattering data can be collected efficiently using a two-dimensional detector, such as an image plate or CCD. In practice, sampling along several curves in reciprocal space is sufficient. These can be measured using a scintillation detector. The primary X-ray beam must be collimated and monochromated to get the desired resolution. Also, the detector's angular acceptance $\Delta\Omega$ (cf. Eq. (9)) has to be minimized to increase the resolution and suppress the background. A typical experimental set up is illus-

trated in Fig. 3.

The momentum transfer q can be controlled by varying the incident and exit angles. Assume that the scattering plane (the plane in Fig. 1) is the (y, z) plane and that ϕ measures the angle between the projection of k_f onto the interface and the y -axis. To a good approximation, the components of the momen-

tum transfer are given in terms of α_i , α_f , and ϕ as

$$\begin{cases} q_x = k \sin \phi \\ q_y = k(\cos \alpha_f - \cos \alpha_i) \\ q_z = k(\sin \alpha_f + \sin \alpha_i) \end{cases} \quad (11)$$

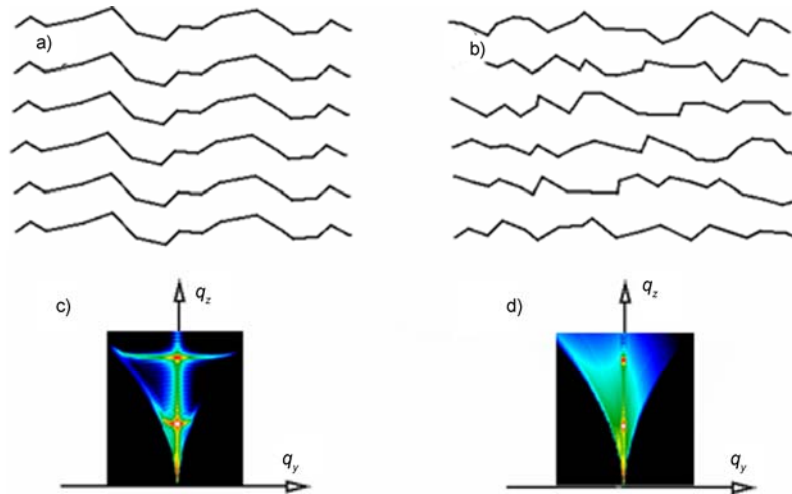


Fig.2 Correlation between interfaces (a) Partially correlated interfaces. The underlying interface structure is partially replicated by the overlayer. (b) Uncorrelated interfaces. The interface contour of the overlayer is not affected by the underlying structure. The intensity distributions in reciprocal space corresponding to (a) and (b) are depicted in (c) and (d), respectively. The interfaces that are of concern in this review are dynamically correlated due to the interactions between them.

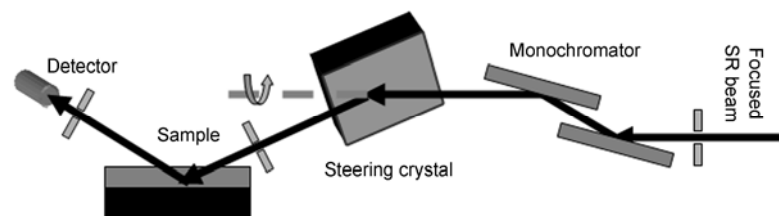


Fig.3 Schematic drawing of a typical experimental set up for X-ray scattering from liquid interfaces. Focused beam from the synchrotron ring is collimated by a slit before hitting the monochromator. The beam is then steered by a steering crystal so that it is incident upon the sample interface at a grazing angle α_i (Fig. 1). The steering crystal rotates around the axis which coincides with the horizontal beam incident upon it (dashed line). The sample is mounted on a vibration-isolation z -stage which controls the sample height according to the steering angle. The scattered photons are collected by a detector which is preceded by a slit to reduce the background scattering.

In the experimental set up, the detector was wide open in the out-of-plane direction to integrate effectively the scattering perpendicular to the scattering plane (along q_x). It was assumed that the angular acceptance $\Delta\phi$ is large enough so that the scattering at angles $\phi > \Delta\phi/2$ can be neglected, therefore the limits on the q_x -integration can be set to $-\infty$ and $+\infty$. This is equivalent to replacing the two-dimensional integration in Eq. (3) by a one-dimensional integration

over y , thereby simplifying the numerical evaluation significantly.

It is seen from Eq. (11) that the specular reflectivity as a function of q_z is obtained by scanning α_i and α_f simultaneously while keeping them equal so that $q_y=0$. This so-called longitudinal scan is equivalent to a θ - 2θ scan in X-ray crystallography. The diffuse scattering is often sampled in one of three ways (Fig. 4). The most frequently used scan is the transverse scan (or rocking scan) which is realized by

scanning α_i and α_f while keeping $\alpha_i + \alpha_f = \text{constant}$. The momentum transfer q_z varies little in such a scan. A second type of scan is the off-specular longitudinal diffuse scan, which is realized by scanning α_i and α_f simultaneously while keeping $\alpha_i - \alpha_f = \Delta\omega$. The off-set angle $\Delta\omega$ is usually very small, but is slightly larger than the width of the central specular peak in the transverse scan. In such a scan, q_z is varying and $q_y = \tan(\alpha_f/2 - \alpha_i/2) \cdot q_z$. The third type of scan is often called the detector scan, which is realized by simply varying the α_f angle while keeping α_i fixed at a small value. The momentum transfer q_y changes rapidly but q_z changes slowly in such a scan. It provides similar information as does the transverse scan and is often used instead of the transverse scan when it is not convenient to change the α_i angle.

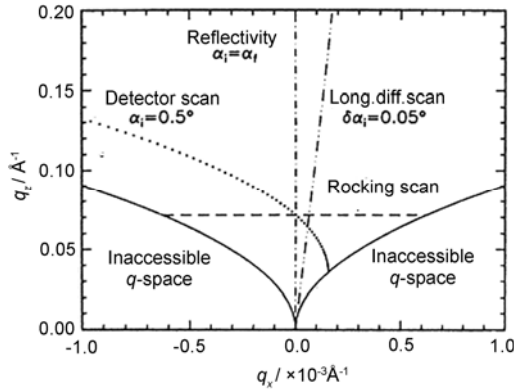


Fig.4 Scans in reciprocal space (q_y , q_z). The scans are defined in the text. The regions below the solid lines are inaccessible for in-plane scattering (figure taken from Ref. [1]).

4 Alkane-water interfaces^[4-6]

We begin with neat liquid-liquid interfaces. Wave excitations are always present at liquid-liquid interfaces. Here, the interest lies in the capillary waves due to thermal excitation. The interfacial free energy is proportional to the area of the interface:

$$F = \gamma \int dx dy \sqrt{1 + h_x^2 + h_y^2} + \frac{1}{2} \Delta\rho_m g \int dx dy h^2(x, y) \quad (12)$$

where γ is the surface energy per unit area, $h_x = \partial h / \partial x$, $\Delta\rho_m$ is the difference between the mass densities of the two phases, and g is the gravitational acceleration. The second integration in Eq. (12) accounts for the gravitational energy required to move the interface up and down. The amplitudes of the capillary waves are much smaller than their wavelengths;

therefore, Eq. (12) can be approximated by

$$F = \gamma A + \frac{1}{2} \gamma \int dx dy (h_x^2 + h_y^2) + \frac{1}{2} \Delta\rho_m g \int dx dy h^2 \quad (13)$$

where A is the area of the flat interface. The statistical mechanics for this system can be worked out by treating the interfacial free energy as an effective Hamiltonian. Representing $h(\mathbf{r})$ by the sum of its Fourier components, that is, $h(\mathbf{r}) = \sum_{\mathbf{q}} \alpha(\mathbf{q}_{\parallel}) \exp[i\mathbf{q}_{\parallel} \cdot \mathbf{r}]$, and applying the equipartition theorem of statistical mechanics,

$$\langle \alpha(\mathbf{q}_{\parallel}) \alpha(-\mathbf{q}_{\parallel}) \rangle = \frac{k_B T}{\gamma(q_{\parallel}^2 + k_g^2)} \quad (14)$$

the reverse Fourier transform of which yields the height-height correlation function

$$C(r) = \frac{k_B T}{2\pi\gamma} K_0(k_g r) \quad (15)$$

where $k_g = \sqrt{\Delta\rho_m g / \gamma}$ is the inverse of the capillary length and $K_0(r)$ is the modified Bessel function of the second kind of order zero. At distances $r = k_g^{-1}$, the correlation function is well approximated by a logarithmic form

$$C(r) \approx \frac{k_B T}{2\pi\gamma} (-\gamma_E - \log(k_g r / 2)) \quad (16)$$

where γ_E is the Euler's γ constant. A direct consequence of this approximation is that the differential cross section follows a power law:

$$d\sigma/d\Omega \propto q_{\parallel}^{\eta-2} \quad (17)$$

where $\eta = k_B T q_z^2 / (2\pi\gamma)$. Such a power law has been observed experimentally (cf. Fig. 5).

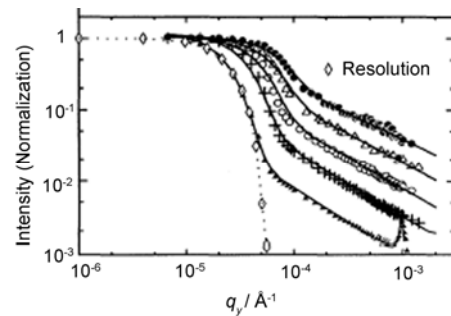


Fig.5 Log-Log plot of the transverse diffuse scattering intensity vs. q_y from a free liquid surface at several values of q_z . The intensity is normalized to unity at $q_y = 0$. The characteristic q_z dependence of the power-law exponent can be seen. The central peak is due to the finite instrumental resolution (figure taken from Ref. [7]).

$C(0)$ gives the interfacial width σ_{cap} due to capillary fluctuations. It is infinite according to Eq. (15),

implying that the mean interfacial plane is not well defined. This is a consequence of the continuous nature of the capillary wave theory. The wavelengths of the capillary waves have a cutoff which sets a limit to σ_{cap} . The effect of the cutoff is accounted for by replacing r in Eq. (15) with $\sqrt{r^2 + r_0^2}$. The cutoff is usually chosen to be of the order of the intermolecular distance. The value of σ_{cap} is insensitive to the exact choice of the cutoff. For example, varying the cutoff length by a factor of 2 results in a change of only 3 % to σ_{cap} . This is the theoretical basis for the interpretation of the reflectivity measurements on alkane-water interface which is a fundamental model system for understanding liquid-liquid interfaces and interactions of alkyl chains with water (Fig. 6).

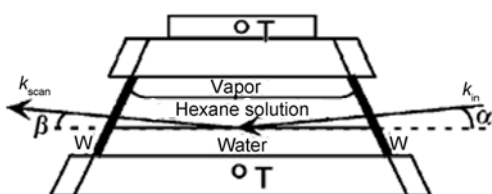


Fig. 6 Cross-sectional view of the sample cell used to measure the X-ray scattering from liquid interfaces. W represents Mylar windows and T represents thermistors to measure the temperature. The windows are slanted 25° from the vertical to reduce the curvature of the interface. The kinematics of surface X-ray reflectivity is also indicated. α is the angle of incidence, and β the angle of scattering ($\beta = \alpha$ for specular reflection). The sample cell is mounted on a vibration-isolation z-stage which controls the sample height during the scans.

Using a sample cell sketch as shown in Fig. 6, precise X-ray reflectivity measurements are made of the interfacial width of neat water-alkane interfaces for a range of n -alkanes from 6 to 22 carbons long [4]. Fig. 7 illustrates the specular reflectivity for such alkanes. The interfacial tension γ for each interface was carefully measured using a Wilhelmy plate. The reflectivity curves were fitted according to Eqs. (7) and (9) using the interfacial width σ as the only fitting parameter. Fig. 8 shows this width for different alkane lengths. The dashed line indicates the capillary-wave prediction for the interfacial width and differs significantly from the values determined from the data. The width, as measured by X-ray reflectivity, is expected to consist of two contributions: an intrinsic width that characterizes the crossover from one bulk composition to the other and a statistical width due to

thermally induced capillary wave fluctuations of the interface. That is, $\sigma^2 = \sigma_{\text{int}}^2 + \sigma_{\text{cap}}^2$. The difference between the measured width and the capillary wave prediction indicates the presence of such an intrinsic width. The other two lines in Fig. 8 are determined by adding the capillary-wave contribution and an intrinsic structural contribution to the interfacial width, σ_{int} . It was proposed that this intrinsic width is determined by the radius of gyration for the shorter alkanes and by the bulk correlation length for the longer alkanes. These measurements are in disagreement with current computer simulations, though it is not clear that the simulations were sensitive to the level of molecular detail probed by the experiments.

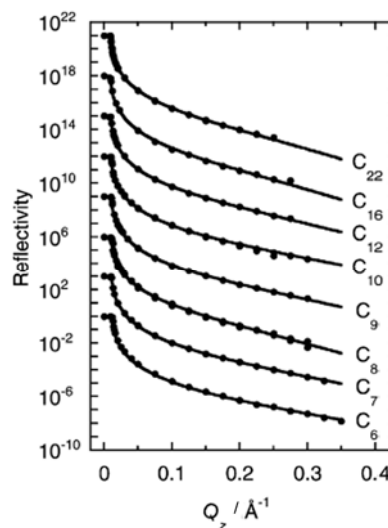


Fig. 7 X-ray reflectivity of the water-alkane interface of eight different n -alkanes (labeled by number of carbons). Curves for the different interfaces are offset for clarity. The solid lines are one-parameter fits to the interfacial width shown in Fig. 8. All the measurements are at 25°C except for the interface with $\text{C}_{22}\text{H}_{46}$ which is at 44.6°C.

The experimental results shown in Fig. 8 indicate that the knowledge of interfaces was poor even for systems as simple as neat liquid-liquid interfaces. X-ray scattering results of surfactant monolayers self-assembled at alkane-water interfaces also yield unexpected structure [5,6]. Gibbs monolayers of soluble surfactants at alkane-water interfaces have a potentially very rich phase behavior, similar to Langmuir monolayers of insoluble surfactants spread on water surfaces. However, the knowledge regarding molecular organization at the liquid-liquid interface is still poor due to a lack of effective structural probes. X-ray reflectivity provided precise measurements of the

electron density and thickness of the monolayer that revealed that the surfactants, near room temperature, are in a close-packed solid phase that fully covers the interface. At higher temperatures, the surfactants undergo a solid to gas monolayer transition at which they desorb from the interface and diffuse into the bulk hexane (Fig. 9).

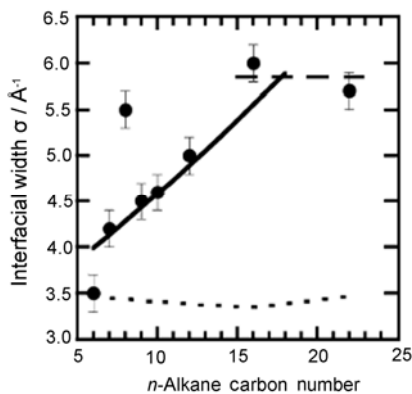


Fig.8 Interfacial width as a function of n -alkane carbon number determined by the X-ray reflectivity measurements shown in Fig. 7. The short-dashed line indicates the prediction for the interfacial width from capillary wave theory. The solid line through the lower carbon number data is determined, without adjustable parameters, by combining the capillary wave contribution with an intrinsic interfacial width determined by the gyration radius of the alkane. The horizontal long-dashed line for the higher carbon numbers is determined by combining the capillary wave contribution with an intrinsic width determined by the measured bulk correlation length of the alkane liquid.

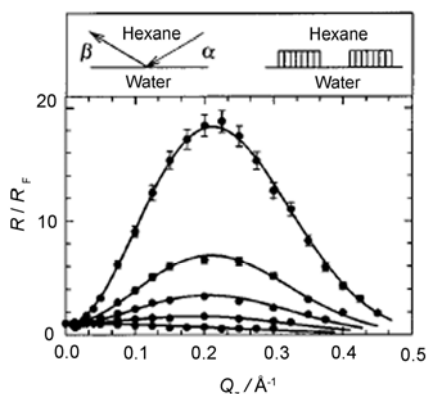


Fig.9 Normalized reflectivity R/R_F vs. Q_z for a $F(CF_2)_{10}(CH_2)_2OH$ monolayer at the water-hexane interface. From the top on down, temperatures are 296.00, 300.75, 309.55, 319.05, and 329.65 K. The intensity of the peak decreases as the temperature rises, implying that the coverage of the interface decreases with increasing temperature. But the reflection maximum remains at $Q_z = 0.21 \text{ \AA}^{-1}$, indicating that the thickness of the monolayer does not change with temperature. Left inset: X-ray scattering geometry. Right inset: cartoon of monolayer domains at water-hexane interface.

Both X-ray reflectivity and diffuse scattering indicated that the solid to gas transition proceeds via a

breakup of the monolayer into solid domains. Reflectivity showed that the electron density profile of the domains is essentially the same as for the lower temperature solid phase that fully covers the interface. Off-specular diffuse scattering produces peaks (small angle surface scattering peaks) from the domains (Fig. 10). Analysis of this scattering revealed that the domain size remains relatively constant ($\sim 1.5 \mu\text{m}$) while the distance between the domains decreases as the interfacial density increases (the latter by more than a factor of ten). The important consequence of this is that domains can be created or destroyed in this system, in contrast to Langmuir monolayers on the water surface for which creation of small domains upon compression is unfavorable.

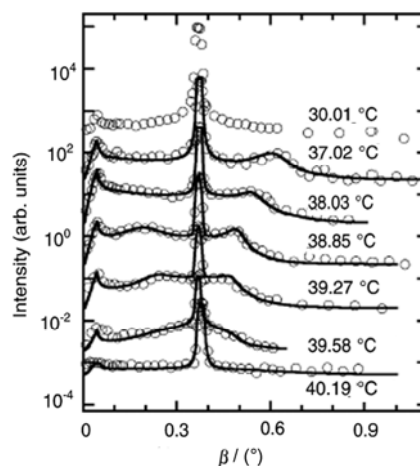


Fig.10 X-Ray diffuse scattering (detector scan) from a monolayer of $F(CF_2)_{10}(CH_2)_2OH$ at the water-hexane interface as a function of temperature. For temperature $T > 40^\circ\text{C}$ the surfactants have desorbed from the interface into the bulk hexane. In this temperature range, the only diffuse scattering is due to capillary waves. For $T < 40^\circ\text{C}$ additional diffuse scattering appears in the shoulders adjacent to the specular peaks. This scattering is due to the formation of monolayer domains consisting of surfactants that have adsorbed to the interface from the bulk hexane solution. The shape of this diffuse scattering was quantitatively analyzed. Fits shown by lines yield domain sizes and distances between the domains. The domain separation decreases upon cooling, as illustrated by the diffuse scattering peaks that move further from the specular peak with decreasing temperature.

5 Aqueous films on aqueous subphases [8, 9]

Wetting phenomena at interfaces are very sensitive to the form of the potential that governs the interaction between the interfaces. Studies of these thin films are useful for understanding the role of short- and long-range forces in interfacial statistical physics.

When two liquid interfaces are placed in close proximity, the interfacial potential creates a coupling between the capillary fluctuations (Fig. 11). This coupling can be simply described by a perturbative modification of the capillary wave Hamiltonian. That is,

$$H = \frac{1}{A} \int d^2r \left\{ \sum_{i=1,2} [\gamma_i (1 + 0.5h_{ix}^2 + 0.5h_{iy}^2) + 0.5g\Delta\rho_{mi}\epsilon_i^2] + 0.5B(h_1 - h_2)^2 \right\} \quad (18)$$

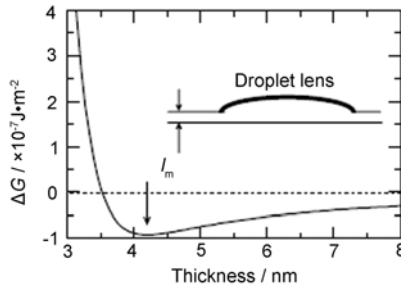


Fig.11 The equilibrium thickness of a partially wetting film corresponds to a minimum in the interfacial potential, or excess free energy of the wetting film, ΔG . This occurs at the point l_m at which $\partial\Delta G/\partial l = 0$. $\Delta G(l)$ is expanded near the minimum to second order, $\Delta G(l) = -C + 0.5B(l - l_m)^2$, to get the coupling constant B between the two interfaces. Inset: Macroscopic lens in equilibrium with a film of thickness l_m (not to scale, cf. Fig. 12).

Using the same mathematics used to derive Eq.

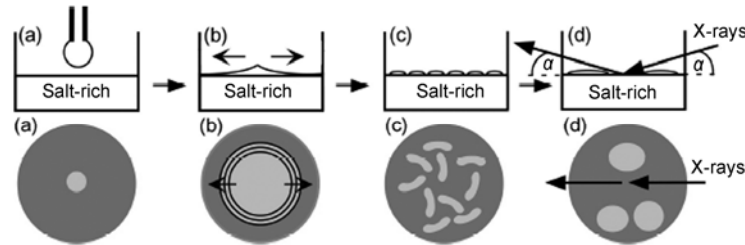


Fig.12 (a) A thin aqueous layer is formed by placing a drop of the PEG-rich phase on the surface of the salt-rich phase with a pipette (top illustrations are side views, bottom ones are top views). (b) Over a period of about one second the drop spreads and a ring of interference colors can be observed. (c) After about 10 seconds, small islands form a spinodal-like pattern (not as ordered as the illustration). (d) The pattern coarsens over a period of about one hour, leaving a few large (approximately one centimeter in diameter) lenses. The lenses are pushed aside with a pipette to allow access for the X-rays that probe the region between the lenses. This region consists of a four nanometer-thick film of a PEG-rich solution.

The X-ray reflectivity demonstrated that a four nanometer-thick film exists in the region between the macroscopic lenses (Fig. 13). This region is a thin layer of the bulk PEG-rich phase, rather than a monolayer of PEG. The widths of the top and bottom interfaces of the film, as determined by X-ray reflectivity, are in agreement with capillary wave theory and the measured interfacial tensions^[8].

X-ray diffuse scattering was used to study quantitatively the coupling between the capillary wave fluctuations on the liquid-vapor and liquid-liquid in-

(14), the canonical average of the correlation functions is obtained in reciprocal space:

$$\langle \alpha_k(q)\alpha_l(-q) \rangle = \frac{2}{A} \times \frac{k_B T X_{kl}}{4M_1 M_2 - B^2} \quad (19)$$

where $X_{11} = M_2$, $X_{22} = M_1$, $X_{12} = B$, and $M_i = B/2 + g\Delta\rho_{mi}/2 + \gamma_i q^2/2$, $i = 1, 2$. The Fourier transform of Eq. (19) is the height-height correlation function of the individual interfaces, $C_{11}(r)$, $C_{22}(r)$, and the height-height cross-correlation function between the two interfaces, $C_{12}(r)$. As expected, as $B \rightarrow 0$ the cross-correlation function $C_{12}(r) = 0$. As $B \rightarrow \infty$ the three correlation functions become identical, indicating complete conformality between the interfacial fluctuations.

To show how X-ray scattering can be used to measure the interfacial interaction of liquid films, a partial wetting film is created in an aqueous bi-phase system consisting of water, polyethylene glycol (PEG), and potassium phosphate by adding a drop of the upper PEG-rich phase to the surface of the lower salt-rich phase (Fig. 12). Such a complex system was chosen because it may function as an environment for the two-dimensional assembly of proteins.

Fig. 14 shows two diffuse scattering curves measured near different Q_z . Fitting the data with Eq.(10) using a correlation function derived from Eq. (21), a coupling constant was determined, $B = 1.4 \times 10^{11} \text{ J} \cdot \text{m}^{-4}$ (cf. Fig. 11). The X-ray measurements combined with macroscopic tension measurements led to an evaluation of an expression for the excess interfacial free energy of the thin film as a function of its thickness d , $\Delta G(d) = S_p \exp[(d_0 - d)/A] - A_{\text{eff}}/12\pi d^2$, where $S_p = 18.7 \text{ mN/m}$, $1 < d_0 < 3 \text{ \AA}$, $A = 2.9 \text{ \AA}$, and $A_{\text{eff}} = 8 \times 10^{-23} \text{ J}$

is an effective Hamakar constant [8]. The first term of the excess free energy is due to entropic repulsion of the fluctuating interfaces, whereas the second term accounts for the van der Waals forces between molecules in the film and in the subphase.

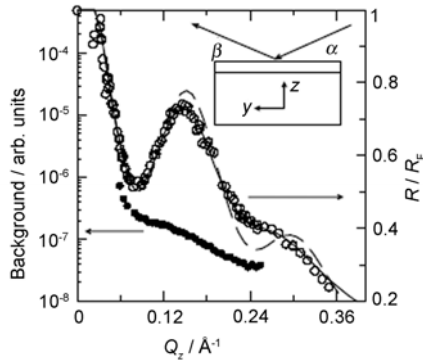


Fig.13 X-ray reflectivity was used to characterize the film thickness and the interfacial widths in agreement with capillary wave theory and the measured interfacial tensions. The reflectivity data are normalized by the Fresnel reflection in order to see the interference fringes more clearly. The background (also called off-specular diffuse scattering in the text) is also presented to show that the fluctuations of the two interfaces are partially correlated. Solid line is the best fit to the data. Dashed line is a calculation assuming that the roughness values of the two interfaces are the same.

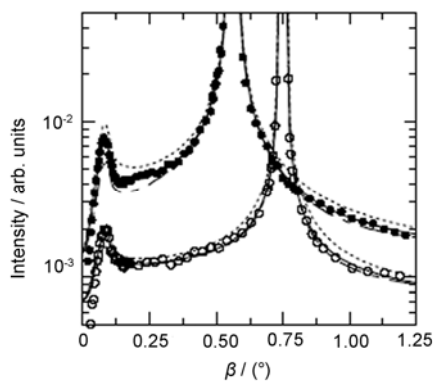


Fig.14 X-ray diffuse scattering (detector scan) as a function of detector angle β demonstrated that the thermal fluctuation of the interfaces are correlated. The measurements were performed at $\alpha = 0.56^\circ$ and 0.79° , respectively. Solid lines are the best fits to the data. Dashed lines are calculations assuming that the thermal fluctuations of the two interfaces are independent of each other. The peak at $Q_z = 0.1 \text{ \AA}^{-1}$ is the so-called Yoneda peak. It appears when β approaches the critical angle for total external reflection. To explain it, a dynamical scattering theory is necessary, which is not discussed in this article but see Refs. [1,2].

Since proteins retain their natural conformation in PEG solutions and protein dimensions are typically similar to the film thickness, it is natural to ask if this thin film can be used to collect proteins into two-dimensional assemblies. In an experiment to test

the proof of this principle, it was demonstrated that ferritin proteins can be assembled into the PEG-rich thin film [9]. Ferritin is used for the storage of iron, and consists of a nearly spherical organic shell surrounding a nearly spherical core in which the iron is stored. The ferritin was prepared in a solution of water and PEG, whose composition mimics that of the PEG-rich solution in the biphasic system. A few drops of the ferritin solution were added to the lower salt-rich bulk phase. Then, they rose to spread into the PEG-rich thin film. The time-resolved measurement revealed the evolution of the film after the addition of ferritin (Fig. 15).

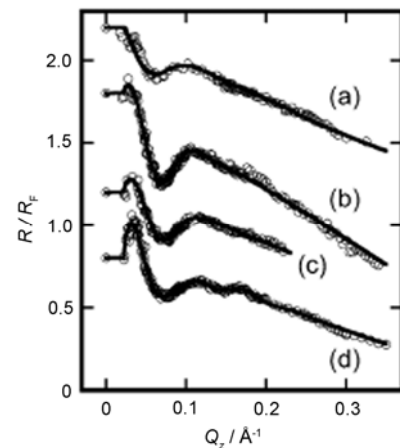


Fig.15 X-ray reflectivity normalized to the Fresnel reflectivity as a function of wave vector transfer for the PEG8000 system (note that the units of R/R_F are relative units; curves are offset for clarity): (a) without ferritin; (b) 1 h after adding ferritin; (c) 18 h after adding ferritin; (d) 36 h after adding ferritin. After 36 h a well-formed ferritin film is present.

Fig. 16 illustrates the electron density profile of this film, as measured using X-ray reflectivity, and compares it to the predicted profile of a layer of ferritin calculated from the known molecular structure of the protein. The near match of measured and calculated profiles indicates that the ferritin forms a two-dimensional film that is ordered normal to the interface.

The overall method described here allows proteins or other biomolecules to be assembled two-dimensionally and studied using X-rays. This is significant because many proteins do not crystallize in three dimensions, or may be difficult to crystallize and, therefore, cannot be studied that way. Allowing proteins to assemble at an aqueous surface often results in protein denaturation, causing the loss of the protein's biological activity. This method retains the natural

shape of the protein at a liquid surface. Moreover, the formation of these two-dimensional arrays may be useful technologically because the arrays allow the biomolecules to interact with other molecules. This could be utilized in chemical sensing or catalytic applications.

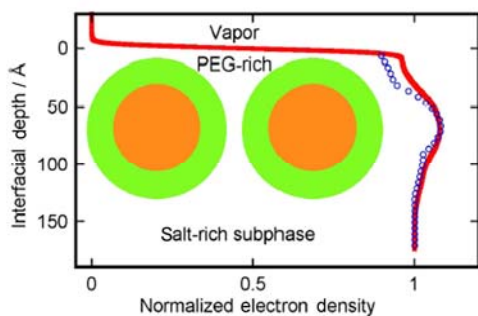


Fig.16 Electron density profile of ferritin adsorbed at the interface between the PEG-rich phase and the salt-rich phase. The solid curve is the profile determined by X-ray reflectivity, and the small circles are a calculation of the profile assuming a single layer of ferritin proteins. The illustration represents (nearly to scale) the position of the ferritin layer used for the calculation. The regions bounded by the two concentric circles represent the core and shell of the ferritin.

6 Lipid bilayers at solid-liquid interfaces [10,11]

Structural studies of biomembranes are difficult, even for pure lipid bilayers, because of strong thermal fluctuations. When deposited on solid substrates, the structure can be easily studied using modern interface-sensitive scattering techniques which use either synchrotron X-rays or neutrons as probes. A high degree of orientation makes possible a precise distinction between the scattering vector component normal and parallel to the bilayer, allowing for the study of questions associated with the lateral structure of the bilayers (Fig. 17). The solid surface effectively reduces the thermal fluctuations, making it possible to get high resolution electron density profiles, even in fully hydrated states.

The X-ray reflection profile contains information on the electron density profile, $\rho(z)$, of the bilayer. Conventional theory cannot reproduce the data at low q_z , where the specular contribution to the θ - 2θ scan is significant. If the specular contribution was included into the data fitting, the resulting electron density profile would deviate greatly from the real one. Kučerka

et al. circumvented this difficulty by combining the analysis of high q_z scattering data from oriented stacks of bilayers with that of low q_z scattering data from extruded unilamellar vesicles [12]. In this approach, one needs small angle X-ray scattering data from vesicles. A different approach is taken to calculate the reflectivity curve. Fig. 18 shows such an example.

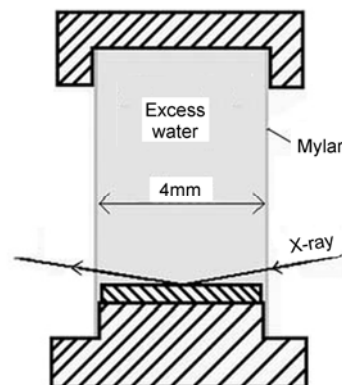


Fig.17 Sketch of the cross section of the sample cell used to study lipid bilayers at solid-liquid interfaces. The solid silicon substrate was located at the bottom of the sample cell. Multilamellar lipid membranes were prepared on a hydrophilic Si(001) substrate. The lipid was dissolved in 1:1 (v/v) chloroform:methanol mixture at a concentration of $50 \text{ mg} \cdot \text{mL}^{-1}$ and pipetted onto the silicon substrate ($4 \text{ mm} \times 10 \text{ mm}$) in a chamber over a period of 12 h. The solution spread spontaneously and the solvent evaporated slowly. The sample was stored in a desiccator for another 24 h at room temperature. It was sealed into the sample cell before X-ray measurements.

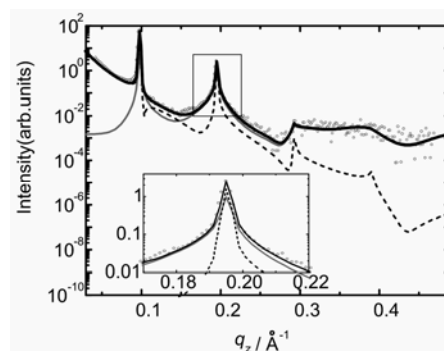


Fig.18 Reflectivity data (symbols) and theoretical calculations (lines) of oriented DOPC multilayer in excess water (Fig. 17). Inset shows how the second Bragg peak is constructed. Although the tails of the Bragg peak are well represented by the conventional theory, the very central peak which arises from the specular reflection is ignored by the conventional theory. Solid black line: the best fit to the data according to the new theory. Dashed line: calculated specular component. Solid grey line: calculated diffuse component.

A new correlation function is introduced in the approach [10,11]. The differential cross section for scattering of X-rays from a stack of lipid membranes at a

solid-liquid interface is the Fourier transform of the electron density profile:

$$\frac{d\sigma}{d\Omega} = r_c^2 \sum_{m,n=0}^N f_m f_n^* e^{iq_z(m-n)d} \int_{-\infty}^{\infty} d^2r e^{iq_{\parallel}r} G_{mn}(r) \quad (20)$$

where $G_{mn}(r) = \exp[-0.5q_z^2 g_{mn}(r)]$ with $g_{mn}(r) =$

$\langle [u_m(r) - u_n(0)]^2 \rangle$ being the height-difference correlation

function between the m-th and n-th bilayer.

$f_0 = \int_{-\infty}^0 \rho_0 \exp[iqz] dz$ and $f_n(q) = \exp[-iq_z d/2] \times$

$\int_{-d/2}^{d/2} \rho(z) \exp[iqz] dz$ are the form factors of the sub-

strate and the bilayer, respectively. Starting from the Hamiltonian of a stack of bilayers and using the boundary condition that fluctuations vanish at the substrate, a correlation function in a simple and analytical form is obtained [10]:

$$g_{ij}(r) = 2\eta \left[\ln\left(\frac{r^2}{4\lambda^2}\right) - \frac{1}{2} \ln\left(\frac{r^2}{8\lambda z_i}\right) - \frac{1}{2} \ln\left(\frac{r^2}{8\lambda z_j}\right) + E_i\left(\frac{r^2}{4|z_i - z_j|\lambda}\right) - E_i\left(\frac{r^2}{4(z_i + z_j)\lambda}\right) \right] \quad (21)$$

where $\eta = k_B T / (8\pi\sqrt{KB})$, $\lambda = \sqrt{K/B}$ and $E_i(x) = \int_x^{\infty} t^{-1} e^{-t} dt$. Eq. (21) helps explain why there is a specular contribution to the reflectivity of a multilayer which is even thicker than 10 micrometers (Fig. 19 for explanation).

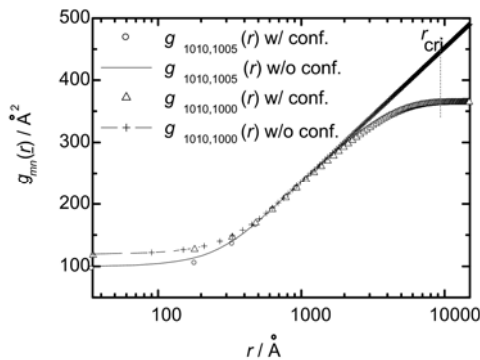


Fig.19 Examples of the height-difference correlation functions for a multilayer with and without confinement by the substrate. The multilayer is composed of about 2000 bilayers. The correlation function of the confined multilayer deviates much from the Caillé correlation function which does not take into account the effect of the substrate. The new correlation functions saturate rapidly when the membranes are close to the substrate. Therefore, $G_{mn}(r)$ in Eq. (20) does not decay to zero as $r \rightarrow \infty$, resulting in specular contributions to the scattering intensity.

The elasticity modulus of the bilayer and the interaction between bilayers are also very important parameters. The parameters B and K in Eq. (21) are the bulk moduli for compression and curvature. They can be determined by fitting the diffuse scattering patterns shown in Fig. 20, which shows the transverse diffuse scans of the multilayer in log-log plot at the first and the second Bragg peak, respectively.

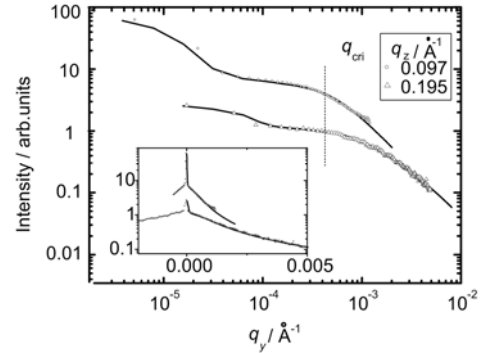


Fig.20 By fitting the diffuse scattering profiles one obtains λ and η in Eq. (21). The diffuse scattering can be roughly divided into two parts, separated by a critical momentum transfer q_{cri} . The diffuse scattering intensity decays faster in large q_y region ($q_y > q_{\text{cri}}$) than in small q_y region ($q_y < q_{\text{cri}}$). The critical momentum transfer q_{cri} corresponds to the critical length scale $r_{\text{cri}} (= 2\pi/q_{\text{cri}})$ in real space (Fig.19). The diffuse scattering profile below q_{cri} ($\sim 2\pi/r_{\text{cri}}$) is mainly due to the geometrical confinement of the substrate on the bilayers. The decay rate in large q_y region is very sensitive to η . On the other hand, λ determines at which point a specific correlation function $g_{mn}(r)$ begins to saturate (cf. Fig. 19). It therefore determines the intensity of the specular reflectivity, too.

7 Summary

X-ray scattering is a useful tool for structural characterization of soft interfaces and fluctuating thin films. Only a few examples of recent studies have been discussed relevant to liquid interfaces. Off-specular scattering is increasingly being used in the study of interface structure in soft materials. Further study on general treatments that combine the effects of small angle scattering with reflectivity is required for a more thorough description. Other surface sensitive techniques, such as Atomic Force Microscopy provide complementary information but are unable to probe buried interfaces noninvasively. Also, owing to current limitations on experimental techniques, few systems have been studied by more than one technique. In the near future, high energy X-ray sources and the further development of neutron reflectivity techniques

can be expected to allow a greater variety of chemical systems to be studied. We look forward to complementary scattering and nonlinear optical measurements that probe different aspects of molecular ordering on the same system.

Acknowledgements

The authors would like to acknowledge their cited collaborators. The research on liquid-liquid interfaces was performed at the University of Illinois at Chicago (with support from the U.S.A. National Science Foundation) and at the National Synchrotron Light Source in Brookhaven National Laboratory (supported by the U.S.A. Department of Energy). The work on solid-liquid interfaces was performed at the Institute of Physics, Chinese Academy of Sciences and at the Beijing Synchrotron Radiation Laboratory. Financial support from the National Natural Science Foundation of China and the Chinese Academy of Sciences are also acknowledged.

References

- 1 Tolan M., X-ray scattering from soft-matter thin films, Springer Tracts in Modern Physics, Vol.148, Springer-Verlag, 1999.
- 2 Holy V., Pietsch U., Baumbach T., High-resolution x-ray scattering from thin films and multilayers, Springer Tracts in Modern Physics, Vol.149, Springer-Verlag, 1999.
- 3 Libbert J L., Pindak R., Dierker S B., *et al.* Phys. Rev. B, 1997, **56**: 6454.
- 4 Mitrinovic D M., Tikhonov A M., Li M., *et al.* Phys. Rev. Lett. 2000, **85**:582.
- 5 Li M., Tikhonov A M., Schlossman M L., Europhys. Lett. 2000, **58**: 80.
- 6 Tikhonov A M., Li M., Schlossman M L., J. Phys. Chem. B, 2001, **105**: 8065.
- 7 Sanyal M K., Sinha S K., Huang K. G., *et al.* Phys. Rev. Lett. 1991, **65** : 628.
- 8 Li M., Tikhonov A M., Chaiko D J., *et al.* Phys. Rev. Lett. 2001, **86**: 5934.
- 9 Li M., Chaiko D J., Schlossman M L., J. Phys. Chem. B, 2003, **107**: 9079.
- 10 Hu S X., Li X H., Jia Q J., *et al.* J. Chem. Phys. 2005, **122**: 124712.
- 11 Li D P., Hu S X., Li M., Phys. Rev. E, 2006, **73**: 031916. Kučerka N., Liu Y F., Chu N J., *et al.* Biophys. J. 2005, **88**: 2626.